J. Fluid Mech. (1982), *vol.* 119, *pp.* 91–105
Printed in Great Britain

Mass transfer between a plane surface and an impinging turbulent jet: the influence of surface-pressure fluctuations

By K. KATAOKA, Y. KAMIYAMA, S. HASHIMOTO AND T. KOMAI

Department of Chemical Engineering, Kobe University, Kobe 657, Japan

(Received 16 January 1981)

Local measurement of the mass-transfer rate and velocity gradient when an axisymmetric jet impinges on a flat plate was carried out using an electrochemical technique. Local measurement of the surface pressure on the flat plate was carried out separately using piezoelectric pressure transducers. The stagnation-point mass-transfer coefficient reaches a maximum when the flat plate is placed at 6 nozzle diameters from a convergent nozzle. It has been confirmed that the mass transfer to the flat plate for a high Schmidt number is greatly enhanced owing to the velocity-gradient disturbances in the wall region of the boundary layer, while the momentum transfer is insensitive to such disturbances. The relative intensity of the velocity-gradient fluctuations on the wall has an extremely large value at and near to the stagnation point, and decreases downstream, approaching a large constant value.

These velocity-gradient disturbances are not due to the usual interaction of Reynolds stress with the shear stress of the mean flow, but are due to the interaction with the surface-pressure fluctuations converted from the velocity fluctuations of the oncoming jet.

The three co-ordinate dimensions of large-scale eddies are calculated from the auto- and spatial correlations of the surface-pressure fluctuations. It is considered that such large-scale eddies play an important role in the production of a velocity-gradient disturbance in the wall region of the boundary layer from the velocity turbulence of the approaching jet.

1. Introduction

As in the case of cross flow around cylinders, the rates of heat and mass transfer across the boundary layer developing from the stagnation point of submerged impinging jets are increased greatly, owing to the so-called free-stream turbulence, compared with theoretical predictions for the turbulence-free condition. Non-uniform distributions of velocity and turbulence in the oncoming free jet make it difficult to analyse the enhancement of heat and mass transfer in the impingement region. The linearization technique for theoretical analysis cannot be used owing to the relative intensity of free-stream turbulence being far larger than that of artificially induced turbulence in channel flows.

Donaldson, Snedeker & Margolis (1971) proposed a model for correlating the impingement heat-transfer rates by applying an empirical turbulent-correction factor to the laminar value calculated for a flow having the same pressure distribution as

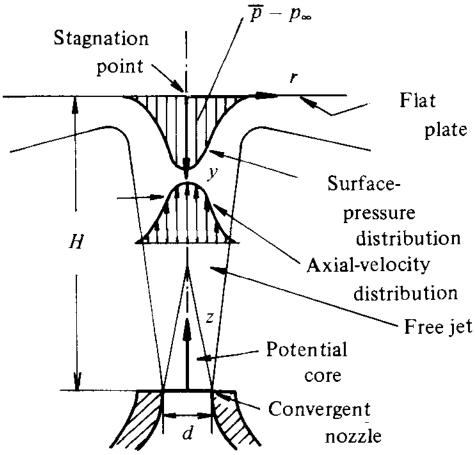

FIGURE 1. Flow configuration and the co-ordinates used.

that present in the impingement region. Chia, Giralt & Trass (1977) also proposed a semi-empirical enhancement factor based on the local axial turbulence intensity at the beginning point of the impingement region.

There is little work on the disturbances within the boundary layer where heat and mass transfer takes place. Kestin and his co-workers (e.g. Sutera, Maeder & Kestin 1963; Kestin & Wood 1970) proposed the vorticity-amplification theory for the heat-transfer enhancement in the cross flow around a circular cylinder, and found discrete cellular vortices arrayed along the stagnation line of a circular cylinder, the axes of which were parallel to the main flow. Yokobori, Kasagi & Hirata (1977) used a flow-visualization technique, and observed an unsteady appearance of large-scale vortices, the axes of which were perpendicular to the stagnation line of two-dimensional submerged jets. However, they did not find a similar vortex structure for an axisymmetric impinging jet. The direct reason for the enhancement of heat and mass transfer remains to be observed. Kataoka & Mizushina (1974) and Kataoka, Komai & Nakamura (1978) measured local values of the velocity gradient and mass-transfer rate on a flat plate using an electrochemical technique. They made an attempt at explaining the local enhancement of mass transfer in terms of the turbulence in the very thin concentration boundary layer for high Schmidt numbers. In their spectral analysis the characteristic frequency that plays a predominant role in the transfer enhancement was found to increase with the square root of the jet Reynolds number. But the exponent of the Reynolds number remains to be checked by more precise correlative analyses. Vallis, Patrick & Wragg (1977, 1978) measured local wall fluxes and wall shear stresses in the wall jet region by means of the same electrochemical technique. Their local Sherwood numbers have the same tendency as those of Kataoka *et al.* in the impingement region. The direct comparison should not, however, be made at different Schmidt numbers until the effect of Schmidt number on the impingement mass transfer is elucidated.

The object of this research is to observe directly the mechanism for the selective enhancement of heat and mass transfer in an axisymmetric impinging jet, and to establish a physical model for it. The electrochemical technique was used to measure the enhanced mass-transfer rates and the velocity gradients on the flat plate. This paper calls attention to the role of the surface-pressure fluctuations in the production of velocity disturbances in the wall region of the boundary layer. Piezoelectric pressure transducers were used to measure the surface-pressure fluctuations on the flat plate. Figure 1 shows the flow configuration and the co-ordinates used.

2. Experimental apparatus and procedure

2.1. *Experiment for mass transfer and fluid-friction measurement*

Local rates of the mass transfer and local values of the velocity gradient on the flat plate were measured using the electrochemical technique developed by Hanratty (1967) and Mizushina (1971). The apparatus is shown in figure 2.

The working fluid was an aqueous solution having equimolar concentrations (about 0·01 M) of potassium ferri- and ferrocyanide and a 1 M concentration of sodium hydroxide as an unreactive supporting electrolyte. Its Schmidt number was kept constant ($Sc = 1800$) by controlling the fluid temperature. A submerged liquid jet issuing from a circular convergent nozzle with diameter of 28 mm ($d = 0{\cdot}028$ m) and contraction ratio of 1/49 impinged normally on a 315 mm diameter circular flat plate made of PVC plastic. Eight nickel plates 1 mm thick were stuck on the surface of the plate. The central nickel plate (80 mm × 110 mm) served as the main cathode, which had three kinds of small isolated test cathodes for measuring local values of the mass-transfer rate and velocity gradient on the impinging surface. The seven remaining nickel plates surrounding the main cathode served as the anode. The surface area of the main cathode was much smaller than that of the anode (the main cathode/anode area ratio = 2/9), so that the current density at the anode was small enough to observe the enhancing phenomena at the cathode. The layout of the test cathodes on the main cathode and the electrode details are shown in figure 3.

Local measurement of the mass-transfer coefficient k (m/s) was accomplished using 42 circular point cathodes (K-electrode) which were fabricated by inserting 0·3 mm diameter nickel wires concentrically into 0·5 mm inner diameter holes drilled in the wall of the main cathode. The K-electrodes, which were electrically isolated from the surrounding main cathode, were held at the same potential as the main cathode for the following electrode reaction under the diffusion-controlling condition

$$\begin{aligned} &\text{cathode:} \quad \mathrm{Fe(CN)_6^{3-}} + \mathrm{e^-} = \mathrm{Fe(CN)_6^{4-}} \\ &\text{anode:} \quad \mathrm{Fe(CN)_6^{4-}} = \mathrm{Fe(CN)_6^{3-}} + \mathrm{e^-}. \end{aligned}$$

The limiting current density i_{d} (A/m^2) on each K-electrode gives the local mass flux at its position on the impinging surface. Under the diffusion-controlling condition, the mass-transfer coefficient k (m/s) was calculated by the equation

$$k = i_{\mathrm{d}}/FC_{\mathrm{A}},$$

where F is the Faraday constant (= 96500 A s/kg-equiv.) and C_{A} the bulk concentration of $\mathrm{Fe(CN)_6^{3-}}$ in kg-equiv./m^3.

Local measurement of the velocity gradient on the impinging surface was accomplished using 11 rectangular test cathodes (S-electrode), which were fabricated by inserting 0·2 mm thick nickel sheets into 0·7 mm long slits, with width ranging from 2 to 3 mm, normally to the radial main-flow direction in the wall of the main cathode. The velocity-gradient measurement was carried out by measuring the limiting current

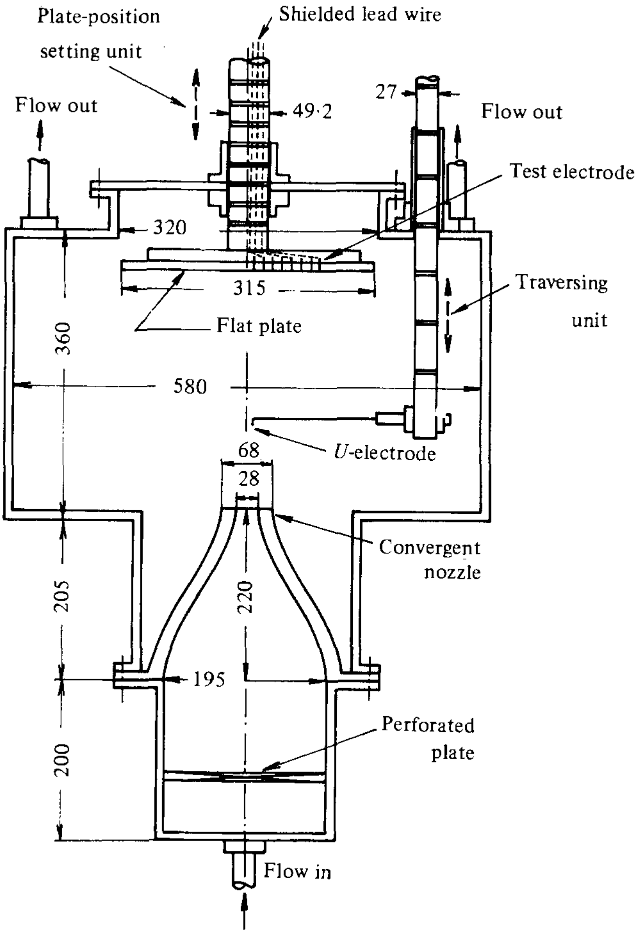

FIGURE 2. Experimental apparatus for mass-transfer and fluid-friction measurement. Dimensions given are in mm.

between each S-electrode and the anode with the main cathode inactive. The limiting current density i_d (A/m^2) on each S-electrode gives the local instantaneous velocity gradient s (s^{-1}) on the impinging surface:

$$s = 1{\cdot}90(i_d/FC_A)^3\,(L/D^2),$$

where L is the streamwise length of the S-electrode and D the diffusivity of $Fe(CN)_6^{3-}$ in m^2/s. This equation is a form of Leveque solution obtained under the assumption of parallel flow. Vallis *et al.* (1977) have pointed out that the velocity-gradient measurement is not appropriate in the impingement region. However, the S-electrode is so short in the flow direction that the radial flow in the boundary layer can be considered to remain unchanged over the surface of the S-electrode. Jolls (1966) has shown that the above equation can be used to approximate the shear stress at the surface of a sphere except in the immediate vicinity of a stagnation point. Local skin friction τ_w (N/m^2) was calculated from the time-averaged measurements of velocity gradient: $\tau_w = \mu\bar{s}$. The relative intensity of the velocity-gradient fluctuations was also calculated from the fluctuating limiting-currents on the S-electrodes.

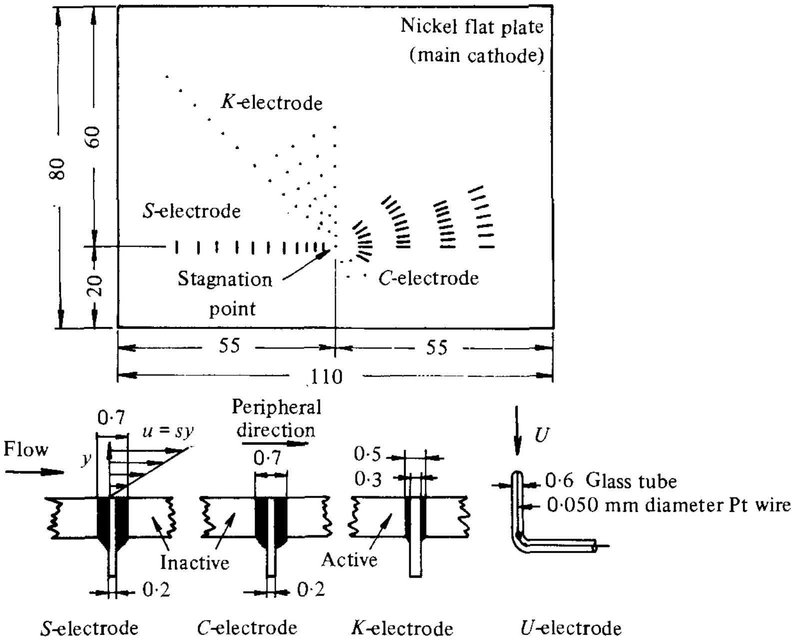

FIGURE 3. Layout of test cathodes and details of the electrodes. Dimensions given are in mm.

Rectangular test cathodes of another type (C-electrodes), which were distributed in the peripheral direction around the stagnation point, were used to see whether a cellular vortex structure exists in the impingement region. However, these C-electrodes were not able to detect any cellular vortex structure similar to that of Kestin & Wood (1970) or Yokobori *et al.* (1977). The whole surfaces of the electrodes were carefully machined and polished to eliminate any roughness and discontinuity on the impinging surface.

A blunt-nose-type electrode (U-electrode) was used to measure the axial velocity of the oncoming jet. As shown in figure 3, the U-electrode was fabricated by fusion of the tip of 0·6 mm outer diameter glass tube into which 50 μm diameter platinum wire had been inserted. The axial velocity U (m/s) was obtained from the limiting current i (A) on the U-electrode: $i = \alpha + \beta U^{\frac{1}{2}}$, where α and β were experimental constants determined by calibration.

2.2. *Experiment for surface-pressure-fluctuation measurement*

The apparatus is shown in figure 4. Local surface-pressure fluctuations were measured simultaneously using two diaphragm-type piezoelectric pressure transducers. A submerged water jet issuing from the same 28 mm diameter convergent nozzle impinged normally on a 315 mm diameter circular flat plate. The flat plate was fixed at 6 nozzle diameters from the nozzle, where the mass-transfer rate at the stagnation point becomes a maximum.

Two pressure transducers were mounted on short swan-neck coupling pipes (1 mm inner diameter) of stainless steel, which connected 1 mm diameter pressure taps for total pressure p (Pa) on the flat plate with a reference pressure tap for static pressure p_∞ (Pa). The transducers were filled with silicon oil, and the coupling pipes with water.

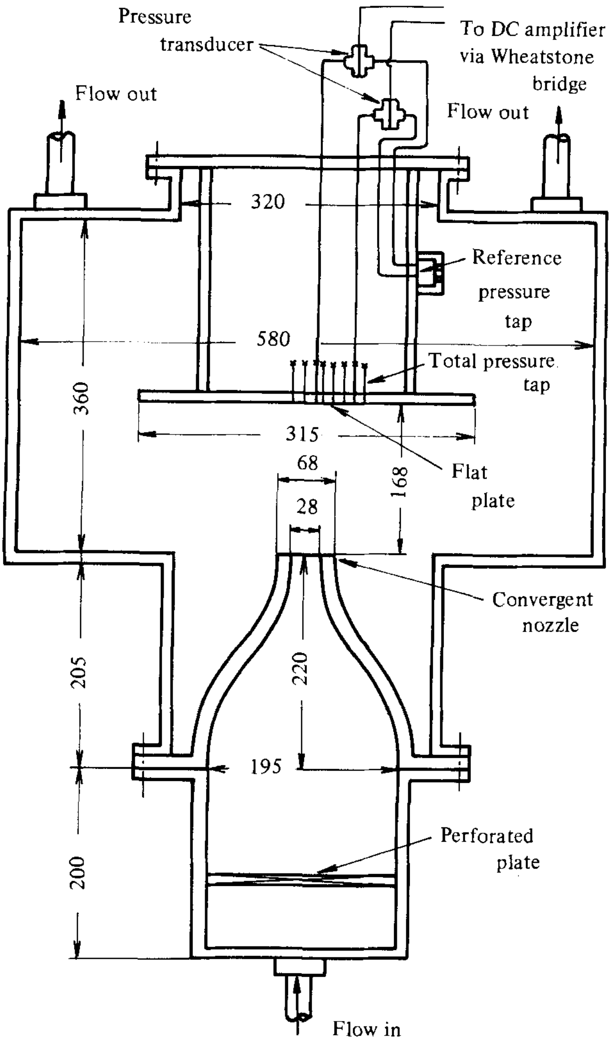

FIGURE 4. Experimental apparatus for surface pressure measurement. Dimensions given are in mm.

The sensitivity of the transducers was approximately 1·9 μV/Pa, and the measurable range was 0–55·2 mV. The relation between the pressure difference $p - p_\infty$ (Pa) and output voltage V (μV) was linear within 0·1 % error: $p - p_\infty = 0{\cdot}526\, V$. The resonant frequency (approximately 600 Hz for air) was much higher than the frequencies to be analysed. The layout of the total pressure taps on the flat plate is shown in figure 5.

Signals from the transducers were fed to the data-processing equipment shown in figure 6. The digital data of the signals sampled at every 2 ms for 20 s by an AD converter were fed into a digital computer.

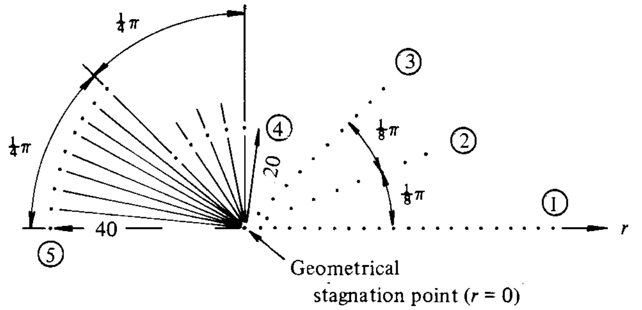

FIGURE 5. Layout of total pressure taps. Dimensions given are in mm. Interval (mm): ①, 3·0; ②, 5·0; ③, 4·0. Interval (rad): ④, $\frac{1}{16}\pi$; ⑤, $\frac{1}{32}\pi$. 1 mm diameter total pressure tap.

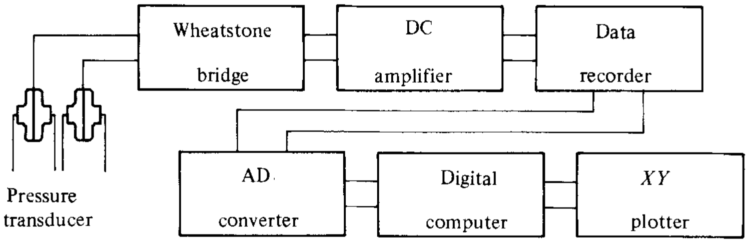

FIGURE 6. Block diagram of the data-processing equipment.

3. Experimental results and discussion

The stagnation-point mass-transfer coefficients are shown as functions of dimensionless nozzle-to-plate distance H/d in figure 7, where the broken line is the theoretical curve of Kataoka & Mizushina (1974) for the turbulence-free condition (the intensity of free-stream turbulence $Tu_f = 0$). Here $Sh_S = k_S d/D$ is the Sherwood number based on the stagnation point mass transfer coefficient k_S, d is the nozzle diameter, D is the diffusivity, $Re_0 = U_0 d/\nu$ is the jet Reynolds number based on the nozzle exit velocity U_0, ν is the kinematic viscosity, and $Sc = \nu/D$ is the Schmidt number.

It is seen from the figure that the rates of mass transfer are greatly increased as compared with their theoretical predictions. The dimensionless mass-transfer coefficient, i.e. the Frossling number $Sh_S/Re_0^{\frac{1}{2}}Sc^{\frac{1}{3}}$, shows a maximum irrespective of Re_0 when the flat plate is placed at 6 nozzle diameters, i.e. $H/d = 6$.

Figure 8 shows the lateral variation of local Frossling number when $H/d = 6$, where r is the radial distance from the stagnation point. The broken line is the corresponding theoretical curve of Kataoka & Mizushina (1974) for the turbulence-free condition. It has been confirmed that the mass transfer is very sensitive to the disturbance in the boundary layer induced by the velocity turbulence of the oncoming jet. A small dip appears in the mass-transfer coefficient at the stagnation point as the last vestige of the effect of the core region, especially when Re_0 is large. It should be noted that the above result has been obtained for only one Schmidt number of 1800. For example, the stagnation-point Frossling numbers calculated from the mass-transfer measurements of Vallis *et al.* (1977, 1978) have the same tendency as those of the present work, but become too small to compare. Therefore direct comparison with other investigations was not attempted.

Figure 9 shows the lateral variation of the dimensionless group of local skin friction $(\tau_w/\frac{1}{2}\rho U_0^2)\,Re_0^{\frac{1}{2}}$ calculated from the measured time-averaged velocity-gradient $\bar{s}$ on the

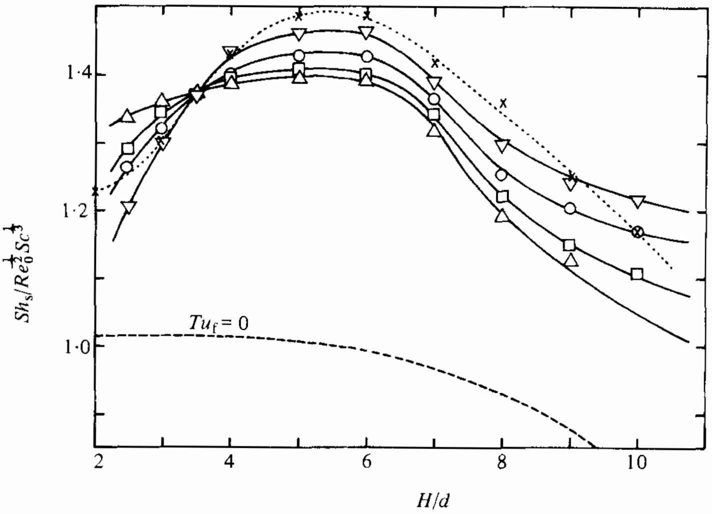

Figure 7. Stagnation-point mass-transfer coefficients as functions of dimensionless nozzle-to-plate distance. △, Re_0 = 4000; □, 6000; ○, 10000; ▽, 15000; ×, Gardon & Cobonpue (1961); Re_0 = 7000, d = 0·009 m (air jet).

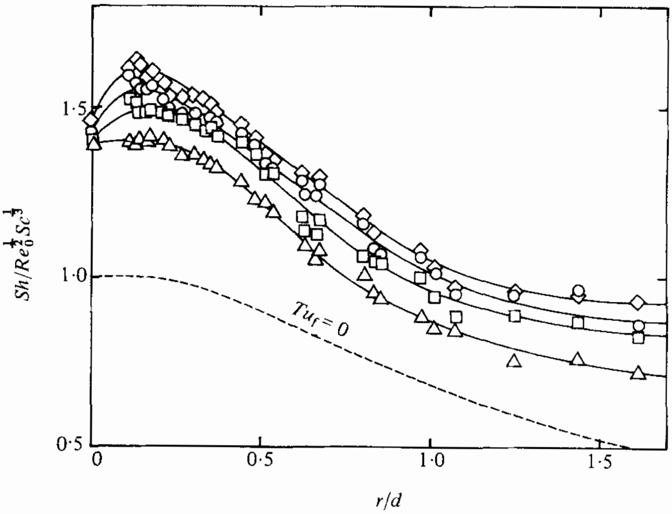

Figure 8. Lateral variation of mass-transfer coefficients when H/d = 6. △, Re_0 = 4000; □, 6000; ○, 10000, ◇, 15000.

impinging surface when $H/d = 6$. Here τ_w is the wall shear stress, and ρ the fluid density. The corresponding theoretical curve of Kataoka & Mizushina (1974) for the turbulence-free condition is in good agreement with the dotted curve obtained from the model of Giralt *et al.* (1977). In the accelerating region, the observed skin friction agrees well with the theoretical curve. This suggests that the momentum transfer is insensitive to the induced disturbances in the wall region of the boundary layer, as distinct from the mass transfer. The relative intensity of the velocity-gradient fluctuations on the wall is also shown in figure 9. It is found that there is no great difference in the relative intensity for various Reynolds numbers. The relative intensity has an extremely large value at and near to the stagnation point, since the time-averaged

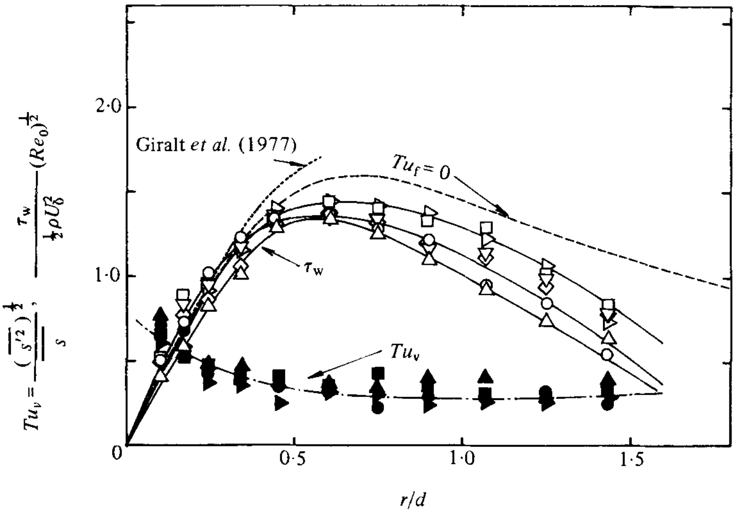

Figure 9. Lateral variation of skin friction and the relative intensity of velocity-gradient fluctuations at the wall when $H/d = 6$. △, ▲, $Re_0 = 4000$; □, ■, 6000; ▽, 8000; ○, ●, 10000; ◇, 12000; ▷, ▶, 15000.

velocity gradient $\bar{s}$ becomes very small there. Even in the downstream region, the relative intensity tends to approach a large constant value of 20–30 %.

According to the boundary-layer analysis of Kataoka & Mizushina (1974), the thickness of the concentration boundary layer for $Sc \sim 10^3$ is about $\frac{1}{10}$ that of the momentum boundary layer. Since the radial velocity u varies almost linearly with the transverse distance y from the wall in the vicinity of the wall, the relative intensities of the velocity-gradient fluctuations $Tu_v = (\overline{s'^2})^{\frac{1}{2}}/\bar{s}$ can be considered as those of the radial velocity fluctuations $Tu_u = (\overline{u'^2})^{\frac{1}{2}}/\bar{u}$ in the concentration boundary layer. As will be mentioned later, the bell-shaped distribution of surface pressure is formed around the stagnation point. The usual generation of velocity turbulence due to the interaction of the Reynolds stress with the shear stress of the mean flow must be suppressed by the steep negative gradient of the surface pressure on the flat plate. It should be considered that the velocity turbulence in the concentration boundary layer comes from the surface-pressure turbulence owing to the jet impingement. It is necessary to observe the characteristic of the surface-pressure turbulence that plays a role in connecting the velocity turbulence of the oncoming jet with the velocity turbulence of the wall region.

Figure 10 shows the time-averaged surface pressure $\bar{p} - p_\infty$ on the flat plate and the intensity of surface-pressure fluctuations $Tu_p^+ = (\overline{p'^2})^{\frac{1}{2}}/(p_s - p_\infty)$ when $H/d = 6$. The lateral distribution of the axial velocity $\bar{U}$ measured at 6 nozzle diameters in the free jet without the flat plate is also plotted for comparison in the same figure. The subscripts s, c, and ∞ indicate respectively the stagnation point, the jet axis, and the surrounding stationary fluid. It is found that the surface-pressure profile almost coincides with the axial-velocity profile, and that the intensity Tu_p^+ has almost as flat a distribution in the impingement region as the intensity of velocity fluctuations of the fully-developed free jet. This suggests that the surface-pressure fluctuations come from the axial-velocity fluctuations of the oncoming jet. The axial component of velocity turbulence U' in the oncoming jet is first converted to the surface-pressure

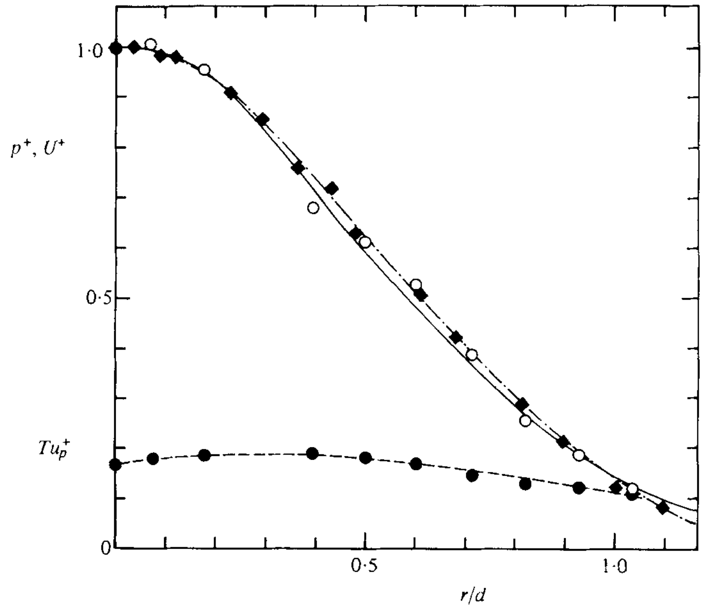

FIGURE 10. Lateral variation of time-averaged surface pressure, the intensity of surface-pressure fluctuations, and the axial velocity of the free jet. ○, $p^+ = (\bar{p}-p_\infty)/(p_s-p_\infty)$; ●, $Tu_p^+ = (\overline{p'^2})^{\frac{1}{2}}/(p_s-p_\infty)$; ◆, $U^+ = \bar{U}/U_c$.

turbulence p' owing to the jet impingement, and then the surface-pressure turbulence produces the radial-velocity disturbances u' in the wall region of the momentum boundary layer.

Since the surface-pressure fluctuations differ in phase at different positions on the flat plate, it is necessary to consider the scale of the surface-pressure turbulence by means of correlative analysis. Lagrangian autocorrelation was evaluated from the surface-pressure fluctuations measured at a fixed point:

$$R_\tau = \frac{\overline{p'(t)\,p'(t+\tau)}}{\overline{p'^2}}, \tag{1}$$

where the overbar denotes a time-averaged value and τ is the time difference. Figure 11 shows the curves of Lagrangian autocorrelation coefficient drawn by an XY-plotter.

The Lagrangian integral time scale was evaluated by integrating the Lagrangian autocorrelation:

$$T = \int_0^\infty R_\tau(\tau)\,d\tau. \tag{2}$$

Figure 12 shows the Lagrangian integral time scale as a function of Re_0. When Re_0 is large enough, i.e. $Re_0 > 9000$, the time scale T is inversely proportional to Re_0, but almost independent of the radial distance r. This suggests that the characteristic frequency in the previous paper (1978) is proportional to Re_0 rather than $Re^{\frac{1}{2}}$. The integral length scale Λ_z in the z-direction can be considered as the product of the integral time scale T and the time-averaged axial velocity $\bar{U}$ of the oncoming jet at the same radial position. Since $\bar{U}$ is proportional to Re_0, $\Lambda_z = \bar{U}T$ should be indepen-

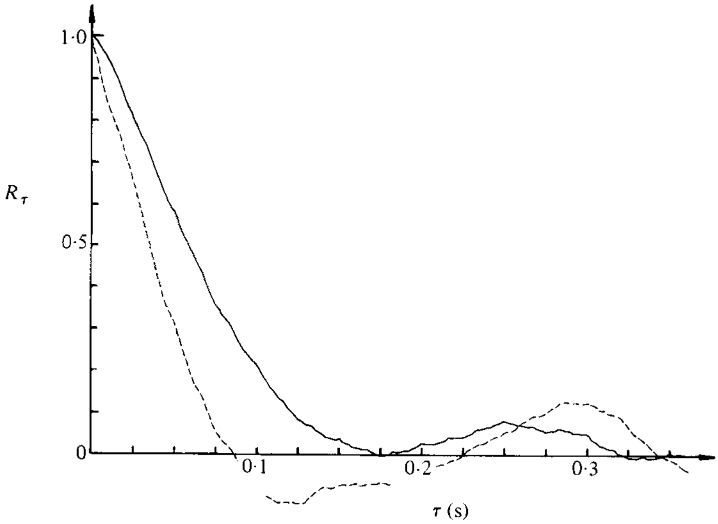

FIGURE 11. Lagrangian autocorrelation coefficients. ——, $r/d = 0$, $Re_0 = 8900$; - - - - -, 0·143, 13900.

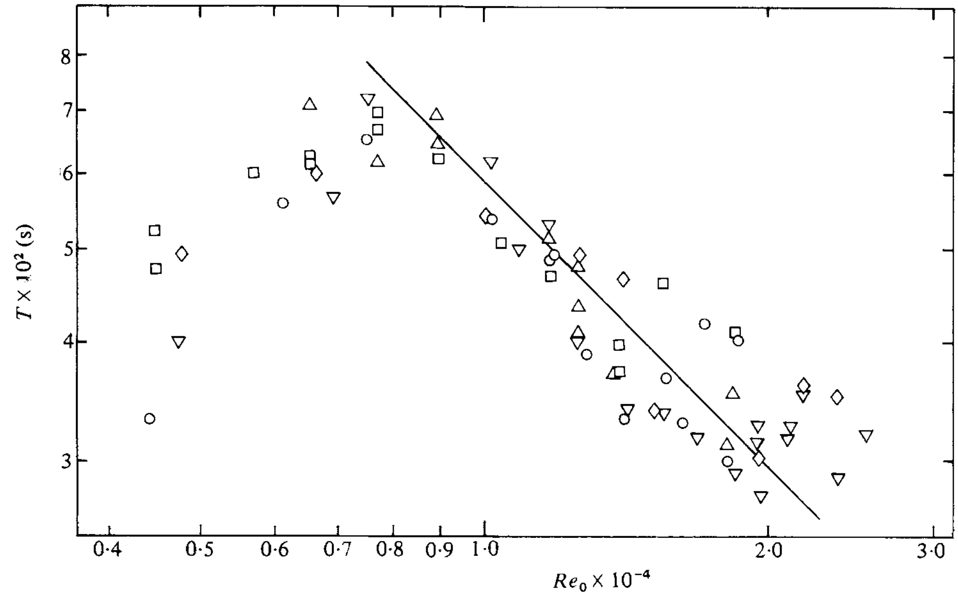

FIGURE 12. Lagrangian integral time scale as a function of jet Reynolds number. △, $r/d = 0$; □, 0·143; ○, 0·178; ◇, 0·357; ▽, 0·743.

dent of Re_0. Although T is independent of r, Λ_z decreases with r at the same rate as $\overline{U}$ decreases.

Spatial correlation was taken at two measuring points (r, θ) and $(r, \theta + \phi)$, which were located at the same radial distance from the stagnation point:

$$R_\phi = \frac{\overline{p'(r,\theta)\,p'(r,\theta+\phi)}}{\overline{p'(r)^2}}, \qquad (3)$$

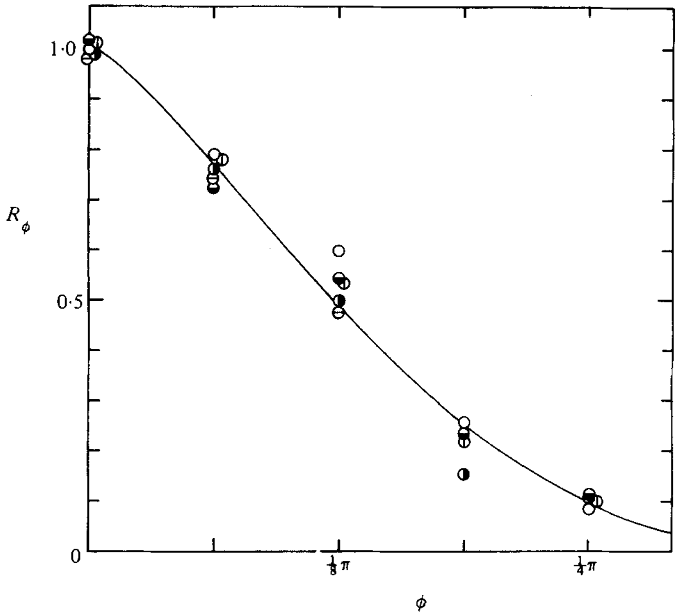

FIGURE 13. Peripheral correlation curves at various jet Reynolds numbers: $r/d = 0{\cdot}714$. ⦶, $Re_0 = 10200$; ◒, 11800; ◑, 14900; ⊖, 17000; ○, 18800.

where ϕ is the angular spacing between two measuring points, and θ the angular coordinate. Figure 13 shows the correlation coefficients for various Reynolds numbers. The correlation curves for various Reynolds numbers coincide with one another. The integral angle scale is defined by

$$\Lambda_\phi = \int_0^\infty R_\phi(\phi)\, d\phi. \tag{4}$$

Integrating the correlation curve, the integral angle scale Λ_ϕ has been found to be approximately $\frac{1}{8}\pi$, irrespective of Re_0. The integral length scale in the θ-direction can be considered to be $r\Lambda_\phi$.

Another spatial correlation was taken at two measuring points (r, θ) and $(r+x, \theta)$ on the same straight line passing through the stagnation point:

$$R_x = \frac{\overline{p'(r)\,p'(r+x)}}{(\overline{p'(r)^2})^{\frac{1}{2}}\,(\overline{p'(r+x)^2})^{\frac{1}{2}}}, \tag{5}$$

where x is the distance between two measuring points. Figure 14 shows the correlation coefficients obtained at various radial positions.

It should be noted that the correlation curves coincide with one another and are symmetric in spite of the accelerating flow region. This suggests that the surface-pressure fluctuations are related to the axial-velocity fluctuations of the oncoming jet rather than to the radial velocity of the external flow in the impingement region. The integral length scale in the r-direction was calculated by the equation

$$\Lambda_x = \int_0^\infty R_x(x)\, dx. \tag{6}$$

It has been found that Λ_x remains constant (approximately 7·4 mm) and independent of r. This value is approximately equal to $\frac{1}{4}$ of the nozzle diameter.

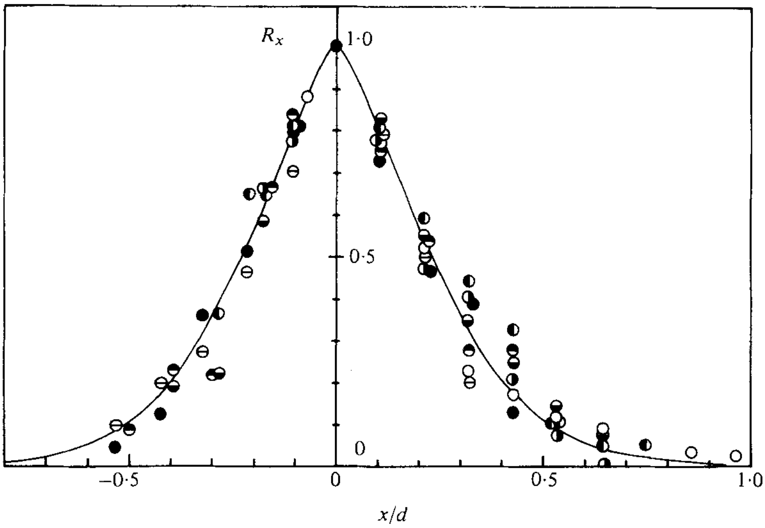

FIGURE 14. Radial correlation curves at various radial positions: $\mathrm{Re}_0 = 12600$. ○, r/d = 0·071; ◑, 0·179; ◐, 0·286; ◒, 0·393; ◓, 0·500; ●, 0·607; ⊖, 0·714.

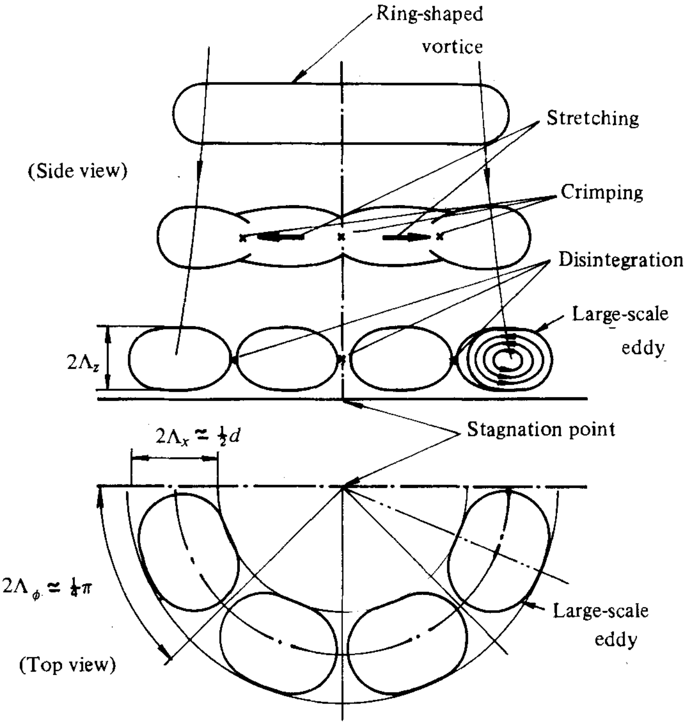

FIGURE 15. Statistical image of the large-scale eddies being produced owing to disintegration of ring-shaped vortices.

It is well-known that instability in axisymmetric free jets develops in the form of ring vortices in the shear layer, and that the turbulence produced in the shear layer diffuses toward the jet axis. From a statistical point of view, the oncoming free jet can be considered to have an axisymmetric turbulent structure. Then the axisymmetric turbulent structure should be distorted and disintegrated in the impingement region owing to the collision of the ring-shaped vortices. Magarvey & MacLatchy (1964) showed some photographs of crimped vortex sheets in the disintegration process of a smoke ring due to collision with a solid plane. Using the above result of three integral scales, the following points can be made regarding the formation of large-scale eddies of the surface-pressure turbulence through the stretching and disintegration of ring-shaped vortices. The integral angle scale Λ_ϕ remains $\frac{1}{8}\pi$. This suggests that the crimping of the ring-shaped vortex filaments occurs statistically every $\frac{1}{4}\pi$ apart in angle in the process of vortex stretching, and large-scale eddies are formed owing to the disintegration of the vortices. As the axial length scale Λ_z decreases downstream, the peripheral spacing $r\Lambda_\phi$ between the crimping points increases with conservation of the vortex volume. The radial length scale Λ_x remains constant over the impingement region.

Figure 15 is a statistical image of the large-scale eddies being produced owing to the disintegration of the ring-shaped vortices. The large-scale eddies of the surface-pressure turbulence play an important role in the production of velocity turbulence in the wall region from the velocity turbulence of the approaching jet flow. This is why heat and mass transfer is selectively much more enhanced in impinging flows than in parallel flows. The surface-pressure fluctuations could not be measured simultaneously with the velocity-gradient fluctuations owing to the erosion problem of the diaphragm of the pressure transducer by the electrolytic solution.

The next step is to observe the interaction of the surface-pressure turbulence with the radial-velocity turbulence near the wall.

4. Conclusion

The stagnation-point mass transfer reaches a maximum when the flat plate is placed at 6 nozzle diameters from a convergent nozzle. Only the mass transfer is enhanced owing to the velocity turbulence in the wall region of the momentum boundary layer, whereas the momentum transfer is insensitive to such disturbances.

The relative intensity of the velocity-gradient fluctuations near the wall, which can be regarded as the relative intensity of the velocity fluctuations in the concentration boundary layer for high Schmidt number, has an extremely large value at and near to the stagnation point, and decreases slightly, approaching a large constant value, downstream of the impingement region. In spite of a steep negative gradient of the surface pressure, the velocity turbulence in the concentration boundary layer is maintained at a high level. The surface-pressure turbulence is generated by the jet impingement from the velocity turbulence of the oncoming jet. It can be considered that the large-scale eddies of the surface-pressure turbulence are formed in the process of the stretching and disintegration of the ring-shaped vortices of the oncoming jet. The large-scale eddies play a leading role in the production of the velocity turbulence in the wall region of the momentum boundary layer, where the mass transfer takes place.

REFERENCES

Chia, C. J., Giralt, F. & Trass, O. 1977 *Ind. Engng Chem. Fundam.* **16**, 28.

Donaldson, C. D., Snedeker, R. S. & Margolis, D. P. 1971 *J. Fluid Mech.* **45**, 477.

Gardon, R. & Cobonpue, J. 1961 In *Proc. Int. Heat Transfer Conf.*, part II, p. 454.

Giralt, F., Chia, C. J. & Trass, O. 1977 *Ind. Engng Chem. Fundam.* **16**, 21.

HANRATTY, T. J. 1967 *Phys. Fluids Suppl.* **10**, S126.

JOLLS, K. R. 1966 Ph.D. dissertation, Univ. Illinois, Urbana, U.S.A.

KATAOKA, K., KOMAI, T. & NAKAMURA, G. 1978 In *Proc.* 2nd *A.I.A.A./A.S.M.E. Thermophysics and Heat Transfer Conf.*, 78-HT-5.

KATAOKA, K. & MIZUSHINA, T. 1974 In *Proc. 5th Int. Heat Transfer Conf.*, FC8.3.

KESTIN, J. & WOOD, R. T. 1970 In *Proc. 4th Int. Heat Transfer Conf.*, FC2.7.

MAGARVEY, R. H. & MACLATCHY, C. S. 1964 *Can. J. Phys.* **42**, 684.

MICHALKE, A. 1964 *Ing. Arch.* **33**, 264.

MIZUSHINA, T. 1971 *Advances in Heat Transfer*, vol. 7, p. 87. Academic.

SUTERA, S. P., MAEDER, P. F. & KESTIN, J. 1963 *J. Fluid Mech.* **16**, 497.

VALLIS, E. A., PATRICK, M. A. & WRAGG, A. A. 1977 *Euromech.* **90**, Nancy, France.

VALLIS, E. A., PATRICK, M. A. & WRAGG, A. A. 1978 In *Proc. 6th Int. Heat Transfer Conf.*, FC(b)-21.

YOKOBORI, S., KASAGI, N. & HIRATA, M. 1977 In *Proc. Symp. on Turbulent Shear Flows*, pp. 3, 17.